23rd Conference of the Italian Association of Aeronautics and Astronautics
AIDAA2015
Politecnico di Torino, 17-19 November 2015
E. Carrera, M. Cinefra, A. Pagani, M. Petrolo and E. Zappino (Editors)
www.aidaa2015.it

NUMERICAL SIMULATION OF FLUIDIC THRUST-VECTORING

Michele Ferlauto[*], **Roberto Marsilio**[†]

[*] Politecnico di Torino
Department of Mechanical and Aerospace Engineering
Corso Duca degli Abruzzi, 24 10129, Torino, Italy
e-mail: michele.ferlauto@polito.it, web page: http://staff.polito.it/michele.ferlauto

[†] Politecnico di Torino
Department of Mechanical and Aerospace Engineering
Corso Duca degli Abruzzi, 24 10129, Torino, Italy
e-mail: roberto.marsilio@polito.it

Keywords: Thrust Vectoring, Dual Throat Nozzles, Computational Fluid Dynamics.

Summary *The paper focuses on a computational method for the investigation of Fluidic Thrust Vectoring (FTV). Thrust vectoring in symmetric nozzles is obtained by secondary flow injections that cause local flow separations, asymmetric pressure distributions and, therefore, the vectoring of the primary jet thrust. The methodology proposed here can be applied for studying numerically most of the strategies for fluidic thrust vectoring, as shock-vector control, sonic-plane skewing and the counterflow method. The computational technique is based on a well-assessed mathematical model. The flow governing equations are solved according to a finite volume discretization technique of the compressible RANS equations coupled with the Spalart-Allmaras turbulence model. Second order accuracy in space and time is achieved using an Essentially Non Oscillatory scheme. For validation purposes, the proposed numerical tool is used for the simulation of thrust vectoring based on the dual-throat nozzle concept. Nozzle performances and thrust vector angles are computed for a wide range of nozzle pressure ratios and secondary flow injection rates. The numerical results obtained are compared with the experimental data available in the open literature.*

Nomenclature

C_d	discharge coefficient of primary nozzle, $\frac{w_p + w_s}{w_{i,p}}$
F_A	nozzle axial force
F_N	nozzle normal force
h_{ut}	height of nozzle upstream throat
h_{dt}	height of nozzle downstream throat
l	length of primary nozzle cavity

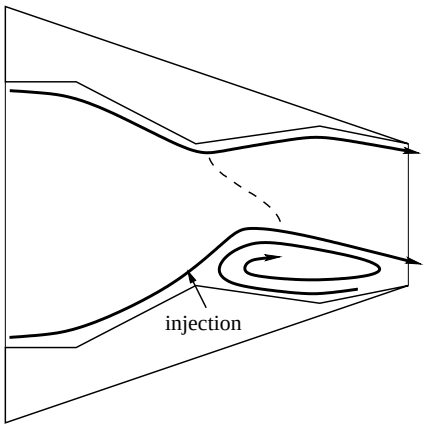

Figure 1: Sketch of the flow mechanism that generates thrust vectoring in the dual-throat supersonic nozzle.

NPR	nozzle pressure ratio, p_t/p_a
p	local static pressure
p_a	ambient static pressure
p_t	primary nozzle total pressure
$w_{i,p}$	ideal weight flow rate of primary nozzle
w_p	weight flow rate of primary nozzle
w_s	weight flow rate of secondary jet
δ_p	resultant pitch thrust vector angle, $\tan^{-1}(F_N/F_A)$
η	resultant pitch thrust vectoring efficiency, $\dfrac{\delta_p}{100 * w_s/(w_s + w_p)}$

1. INTRODUCTION

Thrust Vectoring represents for the aircraft system an additional control variable that offers many benefits in terms of manoeuvrability and control effectiveness [1–3]. Thrust vectoring capabilities make the satisfaction of take-off and landing requirements easier. Moreover, it can be a valuable control effector at low dynamic pressures, where traditional aerodynamic controls are less effective [4–7]. Advantages are also expected for supersonic aircrafts, where the use of thrust vectoring nozzles with a canard airframe configuration is supposed to allow for lower sonic-boom signatures than possible with conventional configurations [6]. Additionally, thrust vectoring could increase conventional controls for some control power to trim the aircraft and thus reduce cruise trim drag [8].

Unlike mechanical thrust-vectoring that use actuated hardware to vector the jet thrust, Fluid Thrust Vectoring (FTV) nozzles use a secondary jet to manipulate the primary air stream. With

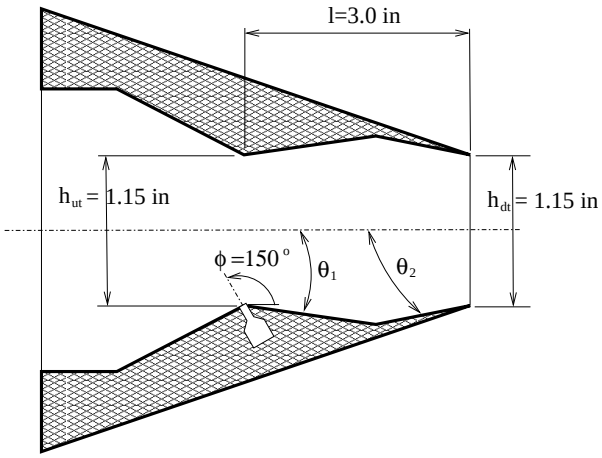

Figure 2: Geometric design variables for the nozzle model tested in Ref. [6] . This nozzle can deflect the primary jet flow backwards only. For actual use, in order to deflect the exit flow upwards, an additional ejection slot is required in the upper wall.

respect to mechanical thrust vectoring the FTV approach does not increase significantly the aircraft weight and it can be also applied to systems that were not designed with such feature.

Some of the mechanisms for thrust vector control include shock-vector control, sonic-plane skewing and counter-flow methods [9, 10]. The shock-vector control method (i.e. the secondary flow injection downstream the nozzle throat) offers substantial vector control but often reduces thrust ratio [5]. Sonic-plane skewing methods (injection at nozzle throat) produce higher thrust ratios but lower resultant thrust vector angles than the shock-vector control method [11]. The counter-flow method (suction in a secondary duct between a primary exhaust nozzle and an aft collar) generates larger vector angles with little secondary flow requirements, but issues need to be addressed such as the installation of a suction supply source, the hysteresis effects, the integration of the system with the airframe [10].

Among different deflection strategies of the nozzle flow, we focused on the Dual-Throat Nozzle (DTN) concept investigated in Ref. [6]. As shown in Figure 1, the nozzle concept is a 2-D convergent-divergent-convergent nozzle with two geometric minimum areas, i.e. the "dual-throat" configuration. A cavity is formed by the nozzle contour between the two geometric minimum areas. The injection slot is located at the upstream minimum area and the asymmetric injection of secondary flow creates a new pattern in the main stream. As depicted in Figure 1, secondary blowing forces the flow to separate in the cavity located on the injection side. The sonic plane becomes skewed, thus vectoring the primary flow. A recirculation bubble forms in the separated-flow cavity and the corresponding wall pressure is pumped down by the primary flow. Conversely, the cavity on the opposite side of the injection slot is filled by the high-pressure fluid. This phenomenon highly enhances the asymmetry of the wall pressure distributions along the upper and lower walls of the nozzle. Therefore, an higher thrust vectoring

effect is obtained by the presence of the cavity regions with respect to the throat skewing alone concept. In the DTN related studies [6,7] many geometries and flow injection settings have been experimentally and numerically tested within this design, and some optimal configurations have been identified,which are able to reach up to 15 degrees of vectoring with very low losses in nozzle efficiency.

Whatever the nozzle configuration and the flow control strategy are used to obtain the thrust vectoring, the dynamic behaviour of the system must be investigated. For this purpose, in present paper a numerical framework for the unsteady simulation of the vectoring nozzle is developed. By using as a reference the work of NASA research group [4,6], we aim to investigate numerically the dynamic response of thrust vectoring system based on the dual-throat nozzle concept. The fully unsteady RANS equations are integrated using a parallel finite volume approach with second order accuracy in both time and space. The code has been developed with particular attention to the unsteady simulation of flow control problems [13] where separated flow, unsteadiness, turbulence modelling and compressibility effects may affect the final solution. The numerical results obtained are compared with the experimental and numerical data available in literature.

2. COMPUTATIONAL MODEL

The main flowfield is simulated using a finite volume discretization of the compressible Reynolds Averaged Navier-Stokes equations (RANS). The one-equation model of Spalart-Allmaras (S-A) [14] is used for the turbulence modelling.

The set of governing equations are written in the compact integral form

$$\frac{\partial}{\partial t}\int_v \vec{W} d\mathcal{V} + \int_{\mathcal{S}} \vec{F}_I \cdot \hat{n} d\mathcal{S} + \int_{\mathcal{S}} \vec{F}_V \cdot \hat{n} d\mathcal{S} = \int_{\mathcal{V}} \vec{H} d\mathcal{V} \tag{1}$$

where $\mathcal{V}$ represents an arbitrary volume enclosed in a surface $\mathcal{S}$. $\vec{W}$ is the hyper-vector of conservative variables, $\vec{F}_I$ and $\vec{F}_V$ are tensors containing the inviscid and the viscous fluxes, respectively.

$$\begin{aligned} \vec{W} &= \{\rho, \rho\vec{q}, E, \tilde{\nu}_t\}^T \\ \vec{F}_I &= \left\{\rho\vec{q}, p\bar{\bar{I}} + \rho\vec{q}\otimes\vec{q}, (E+p)\vec{q}, \tilde{\nu}_t\vec{q}\right\}^T \\ \vec{F}_V &= \frac{\sqrt{\gamma M_\infty}}{\mathrm{Re}_\infty}\left\{0, -\bar{\bar{\tau}}, -\kappa\nabla T - \bar{\bar{\tau}}\cdot\vec{q}, -\frac{\nu+\tilde{\nu}_t}{\sigma}\nabla\tilde{\nu}_t\right\}^T \end{aligned} \tag{2}$$

$\vec{q} = \{u, v, w\}^T$ is the velocity vector, E the total energy per unit volume, M_∞ and Re_∞ are the free-stream Mach number and the Reynolds number, γ is the ratio of the specific heats and finally $\bar{\bar{I}}$ is the unit matrix. The non-homogeneous term $\vec{H}$ is due to the turbulence model:

$$\vec{H} = \left\{0, 0, 0, c_{b1}\tilde{S}\tilde{\nu}_t + \frac{c_{b2}}{\sigma}\left(\nabla\tilde{\nu}_t\right)^2 - c_{w1}f_w\left(\frac{\tilde{\nu}_t}{d}\right)^2\right\}^T \tag{3}$$

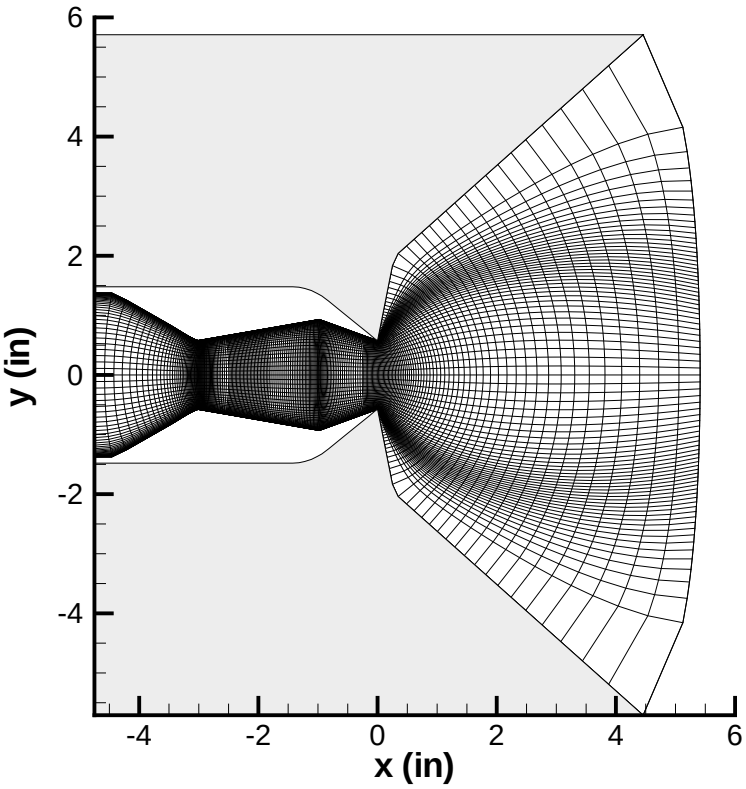

Figure 3: View of the computational domain. The gray zones represent two additional grid blocks required when the interaction with the external flow must be computed. Since the experimental results refer to on-ground tests ($M = 0$) these regions can be replaced by calm-air and constant-pressure boundary conditions.

Turbulent eddy viscosity $\tilde{\nu}_t$ apart, $\vec{H}$ contains turbulence model constants and parameters. The reader is referred to Ref. [14,15] for a full explanation of the model and constants. System (1) is reduced to non-dimensional form with respect to the following reference values: L for length, ρ_∞ for density, T_∞ for temperature, $\sqrt{RT_\infty}$ for velocity, RT_∞ for energy per unit mass and μ_∞ for viscosity. The viscous stresses are written as

$$\tau_{ij} = (\mu + \mu_t) \left[\frac{\partial q_j}{\partial x_i} + \frac{\partial q_i}{\partial x_j} - \frac{2}{3} (\nabla \cdot \vec{q}) \, \delta_{ij} \right] \tag{4}$$

where the laminar viscosity μ is computed via Sutherland's law. The turbulent viscosity $\mu_t = \rho\nu_t$ is computed through the Spalart-Allmaras one-equation model [14].

The numerical solution of system (1) is based on a Godunov method using Flux-Difference Splitting (FDS) techniques and an Essentially Non-Oscillatory (ENO) scheme second order accurate in both time and space. The integration in time is carried out according to a 4th order Runge Kutta scheme. The Boundary Condition (BC) enforcement follows the guidelines of the

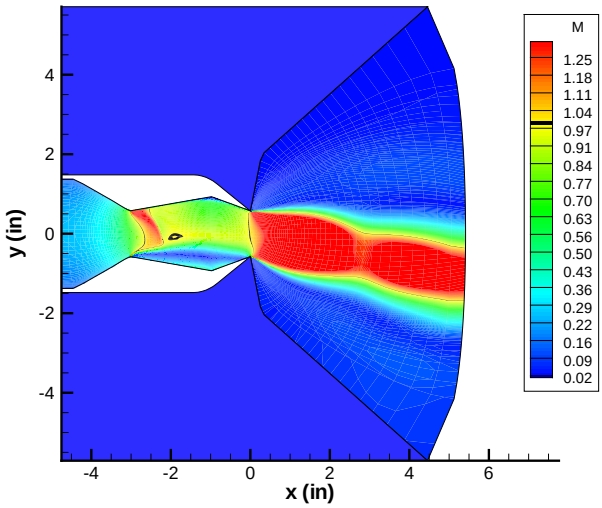

Figure 4: Nozzle flow at the deflected condition with 3% flow injection and $\mathrm{NPR} = 4$. Internal and external nozzle flowfield in terms of Mach number isolines.

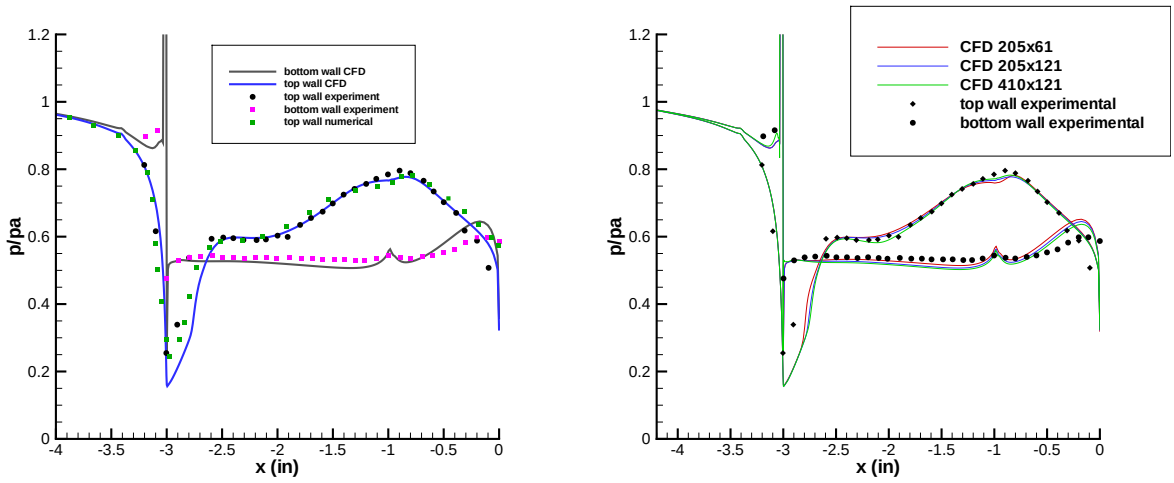

(a) (b)

Figure 5: Nozzle flow at the deflected condition with 3% flow injection and $\mathrm{NPR} = 4$. (a) Comparison of the computed and experimental [6] wall pressure distributions on the nozzle walls; (b) grid refinement study .

characteristic based approach. The numerical details, as well as the code validation, can be found in Ref. [12]. The numerical method has been efficiently parallelized by using OpenMP directives.

2.1 Nozzle geometry

For validating the numerical tool we selected the optimal nozzle configuration designed and tested at Nasa [4–6]. As shown in Figure 2, the nozzle model is 2-D dual-throat nozzle, i.e. characterized by the presence of two geometric minimum areas. The nozzle wide is 4.0 in.

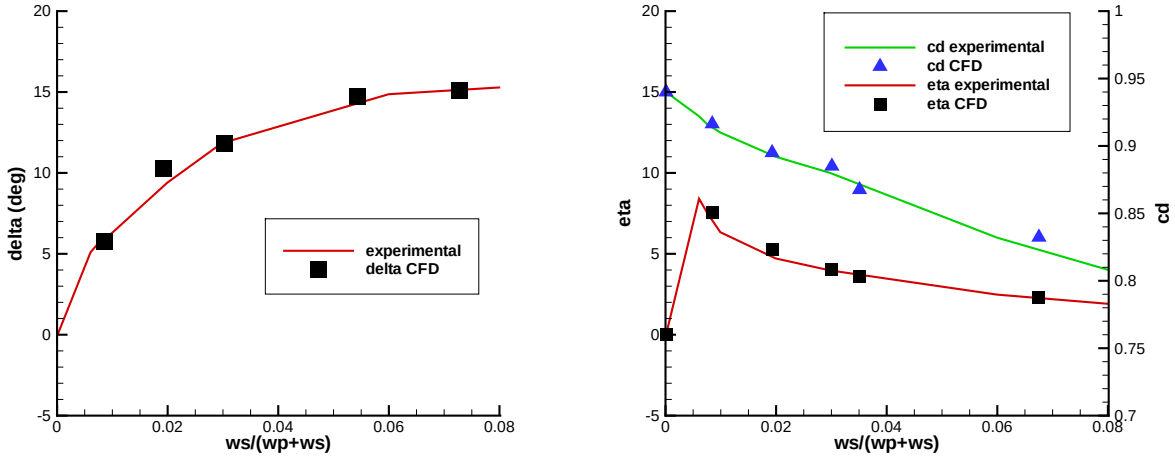

(a) Pitch thrust angle, δ_p

(b) Discharge coefficient C_d

Figure 6: Nozzle performances as a function of the secondary weight-flow ratio at $\mathrm{NPR} = 4$. Comparison between the experimental data [6] and present numerical results (symbols).

The upstream and downstream nominal throat heights are $h_{ut} = h_{dt} = 1.5$ in. The test model has also a nominal upstream and downstream throat areas of 4.6 sq in. The length of the cavity, formed between the two minimum areas, is $l = 3.0$ in. In Ref. [6] different divergent, θ_1, and convergent, θ_2 cavity ramp angles and different injection geometries were tested. We selected the nozzle having $\theta_1 = -10^o$ and $\theta_2 = 20^o$. The secondary flow is injected at the upstream minimum area. The slot injector is placed in the lower part of the nozzle wall, close to the throat. It has a total open area of 0.0864 square inches. Finally, the secondary flow injection angle, ϕ was 150 degrees for all configuration used.

The numerical simulations have been carried out on a 2-D orthogonal structured grid obtained by conformal mapping techniques. Boundary conditions at the computational domain border have been imposed by well assessed techniques according to the FDS approach [12].

The injection flow is simulated by using a modified inlet flow boundary condition. The total temperature and pressure are imposed in order to guarantee the right amount of the ejected mass flow at the slot orifice, while the flow direction must match that imposed by the blowing actuator [13]. These BCs are applied to the cell interfaces belonging to the jet slot.

3. NUMERICAL RESULTS

In this section the numerical results obtained with the proposed modelling approach are presented and the comparison with the numerical and experimental data available in the literature is discussed. Although the simulation of other nozzle configurations and fluidic thrust vectoring approaches can be simulated with present numerical tool, our work focuses on the validation on

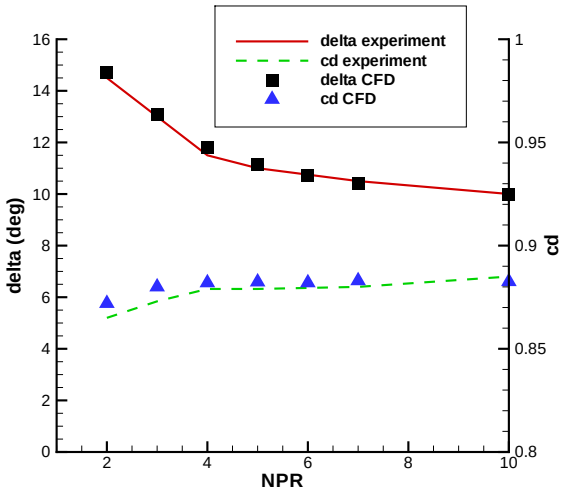

Figure 7: Comparison of experimental and computed deflection angle δ_p and discharge coefficient C_d versus nozzle pressure ratio (3% secondary flow injection).

the dual-nozzle concept. The geometric nozzle configuration used to validate the simulations is that shown in Figure 2. The nozzle flowfliield and performances are simulated while it is operating at different pressure ratio NPR and secondary flow blowing intensities. Grid refinement analyses have been carried out in order to test accuracy and grid convergence.

In Figure 3 an example of the computational domain used in this paper is presented. Since the experimental results [6] refer to on-ground tests ($M = 0$) the interaction of the nozzle jet flow and the external flow can be modelled by far field boundary conditions and the computational domain reduced to a single block structured grid. For the accurate simulation of in-flight conditions, two additional grid blocks are required to compute the external flow (e.g. the zones which are shown in gray in Figure 3).

As first step, the nozzle performances and flowfield are computed at the reference working conditions, that is $\mathrm{NPR} = 4$ and 3% flow injection ($w_s/(w_p + w_s) = 0.03$). The computed steady flowfield is presented in Figure 4 in terms of Mach contours. Figure 4 shows a flow pattern where are clearly visible the lambda foot on the upper divergent cavity wall with the strong shock leading to subsonic flow; the flow separation in the upper cavity apex; the massive flow separation along the lower cavity walls; the plume flow expansion to supersonic flow.

A comparison of the computed pressure distribution at the nozzle walls with the measured data and numerical results of Ref. [6] is presented in Figure 5a. As visible the numerical and the experimental pressure data are remarkably in good agreement.

A grid-refinement study has been also performed to evaluate grid convergence and solution consistency. Solutions were tested on three different grid sizes (205×61, 205×121 and 410×121 points) showing very small changes in internal nozzle performance parameters and thrust vector angles, with a good agreement in terms of wall pressure distribution, (see Figure 5b). The medium mesh (205×121 points) was deemed more than sufficient for estimating performance

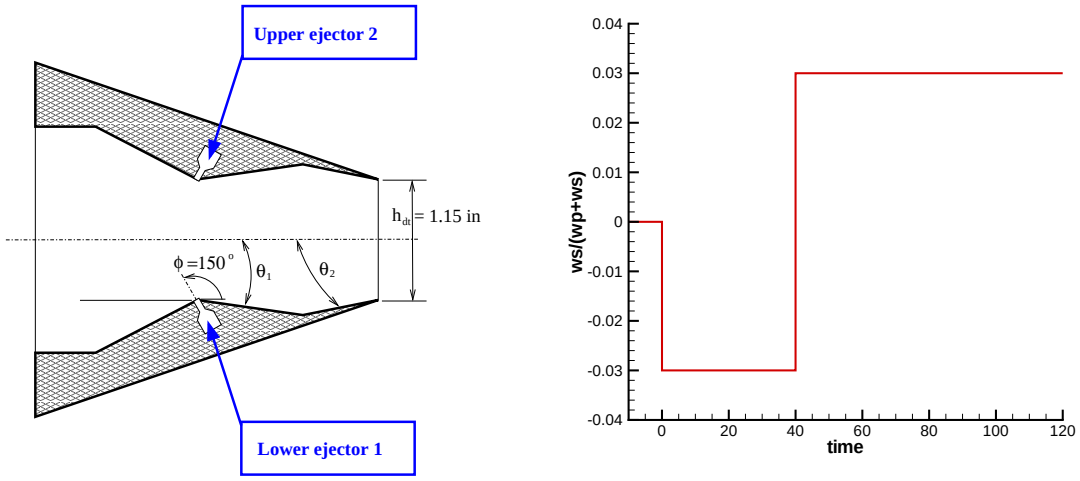

(a) (b)

Figure 8: (a) Sketch of the nozzle actuation setup and (b) desired mass-flow rate during the transient of nozzle vectoring. Flow rates must be always considered in their absolute value. Negative values mean that the lower ejector is active, positive values means that the upper ejector is on.

trends and adequate for predicting performance magnitudes.

The analysis of the nozzle performances follows by varying the strength of the secondary flow injection. In Figure 6 the comparison between the numerical computed, on the 205×121 grid, with the experimental data, in terms of the nozzle internal performances as a function of the secondary weight-flow, $w_s/(w_p + w_s)$. In very good agreement with experimental data presented in [6], the computational results verify that increasing the secondary weight flow ratio (w_s) significantly increases the resultant pitch thrust angle δ_p. All the numerical computed nozzle performances in terms of δ_p, C_d and η compare very well with the experimental data reported in Ref. [6].

Another series of computations have been performed in order to investigate the numerical prevision of the nozzle performances at different pressure ratios. Simulations of the present DTN configuration operating at NPR values ranging from 2 to 10 have been performed. The secondary flow injection has been maintained at the 3% level. The comparison of the predicted results with the experimental data, from Ref. [5], for discharge coefficient and thrust vector angle are shown in Figure 7. Again, the computational results did accurately fit the experimental data.

The numerical results proposed above, have shown that the approach correctly captures the steady state performances of the DTN thrust vectoring system. The proposed method is time accurate, and it can be used therefore to simulate the system dynamics. For actual use, that is, in order to deflect the exit flow both upwards and downwards, at least two ejection slot are

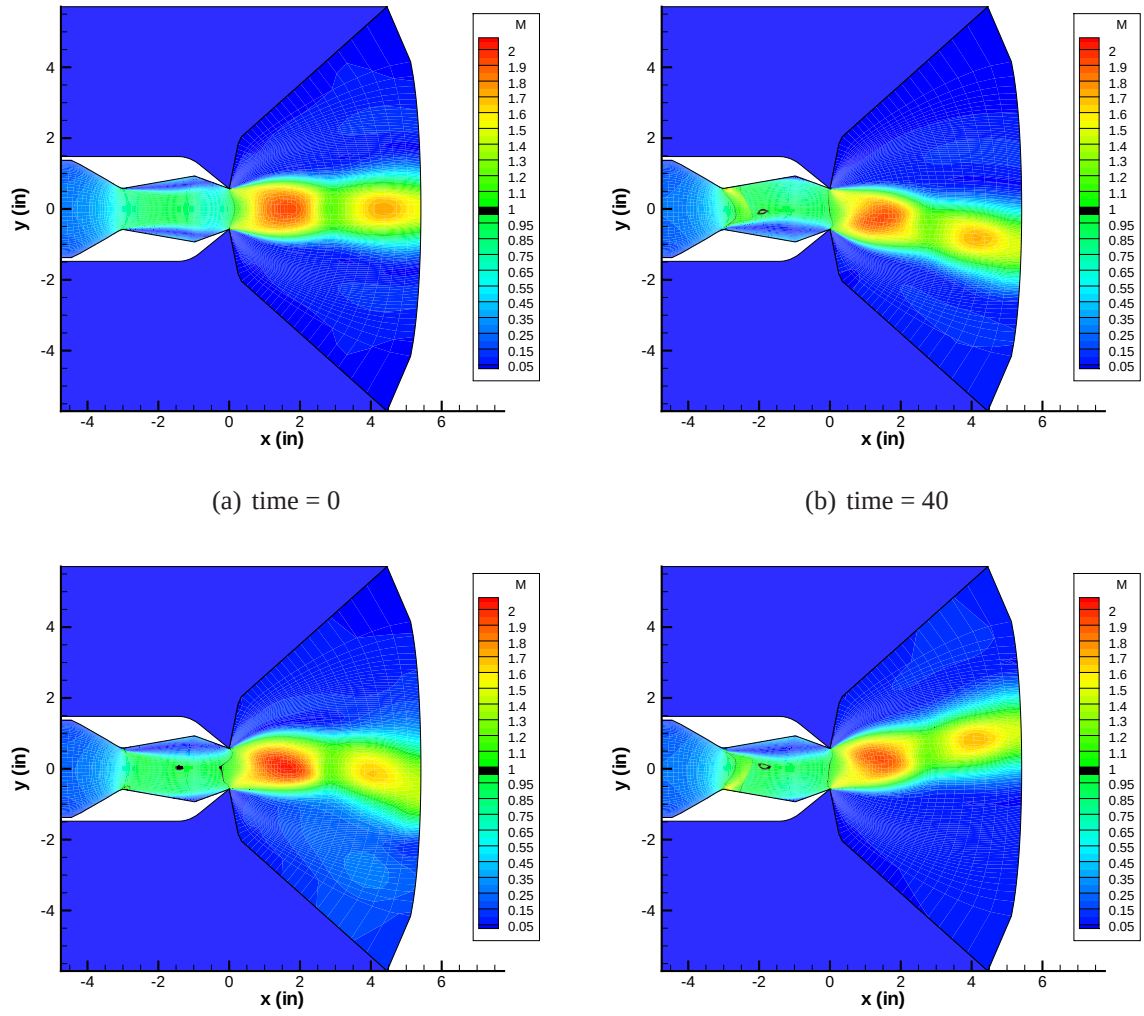

(a) time = 0

(b) time = 40

(c) time = 80

(d) time = 120

Figure 9: Snapshots of the Mach field evolution during primary jet vectoring according to control law of Figure 8b. Starting from the symmetric configuration (a), the jet is deflected backwards (b) and then upwards (c), towards the final condition (d) .

required: one on the upper nozzle wall and one on the lower. The nozzle system is then modified as depicted in Figure 8a.

As an example, the simulation of the active control of the nozzle thrust vectoring is proposed. The control law of the target injection in time is shown in Figure 8b . Briefly, starting from the unmanipulated, symmetric flow on the nozzle (see Fig.9a), the lower actuator is activated with step input at the 3% injection level. When the transient vanished, the deflected condition is reached and, at the adimensional time level $t = 40$, the lower jet-slot is switched off, while the upper actuator is activated, again at the 3% injection flow rate. Figure 9 shows some snapshots of the transient flow pattern during the system dynamic response to the control input function represented in Figure 8b .

4. CONCLUSIONS

A computational tool for the investigation of fluidic thrust vectoring strategies has been presented. FTV uses fluidic injection to manipulate the flow separation inside the fixed nozzle and to cause an asymmetric wall pressure distributions and, therefore, thrust vectoring. The numerical method has been validate for the complex case of the manipulated flow on the supersonic dual-throat nozzle tested at NASA Langley Research Center [6]. This nozzle concept enhances the TV efficiency of sonic-plane skewing by generating a cavity flow system downstream of the nozzle throat that maximizes the pressure differentials between upper and lower wall. The numerical tests were quite severe since the computational tool was dealing with flowfields having a very complex and nonlinear dynamics generated by the strong interactions between moving shocks, boundary layers and separated flow regions. An extensive analysis has been carried-out, in order to validate the code and to verify the correctness of the numerical prevision of the nozzle thrust-vectoring performances. The numerical results obtained have shown a very good agreement with the experimental data published in the open literature for a wide range of the nozzle pressure ratio and secondary flow injection rates. The numerical method here presented is also suitable for the extensive analysis of the nozzle control. As an example, the simulation of the unsteady fluid dynamics of the DTN thrust vectoring in closed-loop control has been briefly illustrated.

ACKNOWLEDGEMENTS

Computational resources were provided by hpc@polito.it, a project of Academic Computing within the Department of Control and Computer Engineering at the Politecnico di Torino (http://www.hpc.polito.it).

REFERENCES

[1] Asbury, S. and Capone, F., High-Alpha Vectoring Characteristics of the F-18/HARV, *Journal of Propulsion and Power*, Vol. 10, No. 1, 1994.

[2] Wilde, P., Crowther, W., Buonanno, A., and Savvaris, A., Aircraft Control Using Fluidic Maneuver Effectors, *26th AIAA Applied Aerodynamics Conference, AIAA paper 2008-6406*, 2008.

[3] Mason, M. and Crowther, W., Fluidic Thrust Vectoring for Low Observable Air Vehicles, *2nd AIAA Flow Control Conference, Portland, OR. AIAA paper 2004-2210*, 2004.

[4] K.A. Deere. Summary of fluidic thrust vectoring research conducted at NASA Langley Research Center. *AIAA paper 2003-2800*, 2003.

[5] K.A. Deere, B.L. Berrier, J.D. Flamm, and S.K. Johnson. A Computational study of new dual throat fluidic thrust vectoring nozzle concept. *AIAA paper 2005-3502, 41rd AIAA/ASME/SAE/ASEE Joint Propulsion Conference & Exhibit*, 2005.

[6] J.D. Flamm, K.A. Deere, M.L. Mason, B.L. Berrier, and S.K. Johnson. Design enhancements of the two-dimensional, dual throat fluidic thrust vectoring nozzle concept. *3rd AIAA Flow Control Conference, San Francisco, CA, United States*, pages 1795–1821, 2006.

[7] K.A. Deere, J.D. Flamm, B.L. Berrier, and S.K. Johnson. Computational study of an axisymmetric dual throat fluidic thrust vectoring nozzle for a supersonic aircraft application. *43rd AIAA/ASME/SAE/ASEE Joint Propulsion Conference & Exhibit, AIAA paper 2007-5085*, 2007.

[8] R. Balu, A.G. Marathe, P.J. Paul, and H.S. Mukunda. Analysis of performance of a hot gas injection thrust vector control system. *Journal of Propulsion and Power*, 7:580–585, 1991.

[9] C.J. Anderson, V.J. Giuliano, and D.J. Wing. Investigation of hybrid fluidic / mechanical thrust vectoring for fixed-exit exhaust nozzles. *AIAA paper 97-3148*, July 1997.

[10] J.D. Flamm. Experimental study of a nozzle using fluidic counterflow for thrust vectoring. *AIAA paper 98-3255*, July 1998.

[11] P.J. Yangle, D.N. Miller, K.B. Ginn, and J.W. Hamstra. Demonstration of fluidic throat skewing for thrust vectoring in structurally fixed nozzles. *2000-GT-0013*, May 8-11, 2000.

[12] M. Ferlauto and R. Marsilio. Computation of plug nozzle turbulent flowfields. *Isabe Paper-1185, 15th ISOABE Conference*,Bangalore. India, 2001.

[13] M. Ferlauto, R. Marsilio. A computational approach to the simulation of controlled flows by synthetic jets actuators. *Advances in Aircraft and Spacecraft Science*, 2(1):77-94, 2014.

[14] P. Spalart and S. Allmaras. A one-equation turbulence model for aerodynamic flows. *La Recherche Aerospatiale*, pages 5–21, 1994.

[15] Spalart, P., Johnson, F., and Allmaras, S., Modifications and Clarifications for the Implementation of the Spalart-Allmaras Turbulence Model, *paper ICCFD7-1902, seventh International Conference on Computational Fluid Dynamics (ICCFD7), Big Island, Hawaii*, 2012, pp. 1–11.